Quantitative Thrust Efficiency of a Self-Propulsive Robotic Fish: Experimental Method and Hydrodynamic Investigation

Li Wen, Tianmiao Wang, Guanhao Wu, and Jianhong Liang

***Abstract*—The robotic fish that utilize the body/caudal fin undulatory locomotion has long interested both biologists and engineers. Although a variety of free swimming robotic fish prototypes have already been developed, very few studies addressed the methods for determining quantitative thrust efficiency. In this paper, we propose a novel experimental method that enables the simultaneous measurement of the power, wake flow field, and self-propulsive speed of a robotic fish, which together facilitate a quantitative measurement of its efficiency. Our results show that the optimal thrust efficiency of the robotic swimmer is within the Strouhal number (St) range of $0.3 \leq \mathrm{St} \leq 0.325$ when single-row reverse Karman vortices are produced. Nevertheless, present robotic fish swam at Strouhal numbers outside the optimal region under self-propulsive condition, and produced another type of wake structure: "double-row vortices." We also show that robotic fish that utilize a low amplitude with a large flapping frequency produce higher self-propulsive speeds, whereas a larger amplitude paired with lower frequency results in higher efficiency. Additionally, a peak efficiency value of 31.6% is recored for the self-propulsive robotic swimmer. The general applicability of this experimental method indicates that broader issues regarding thrust efficiency for biomimetic underwater propulsive robots can be quanlitantively measured.**

***Index Terms*—Digital particle image velocimetryn (DPIV), robotic fish, self-propulsive, thrust efficiency.**

I. Introduction

FISH are often assumed to be very efficient swimmers [1]. Biologists and engineers have made considerable effort to examine the thrust efficiencies of swimming robots and live fish. A principle goal in these endeavors is to extract design and kinetic control principles applicable for producing robotic fish with highly efficient propulsion. A variety of free-swimming devices have already been developed based on these discoveries [2]–[8]. Most works of the existing research on thrust efficiency have been conducted through computation, which can be broadly classified into analytical predictions [9] and computational fluid dynamics (CFD) analyses [10]. However, until recently these results lacked experimental validation. The existing experimental studies examining the thrust efficiency of fish-like locomotion were conducted using flapping foils [11], [12]. Nevertheless, the isolated performance of a flapping foil cannot fully represent a swimming fish's, especially the body/caudal fin (BCF) kinetic pattern that characterizes approximately 88% of extant fish families [13]. Members of these families are also widely used as live counterparts for biomimetic underwater vehicles [14].

So what has held back researchers from experimentally measuring thrust efficiency? Conventionally, thrust efficiency describes a relationship between three parameters: the time-averaged undulatory power consumed by the fluid P_{fluid}, the time-averaged thrust force T_f, and the fish swimming speed U. The measurement of the power consumption of fish-like locomotion has been reported in several previous studies [15]–[17]. For robotic applications, a commonly used approach is to subtract the transmission power from the total power consumed by the motors as they actuate the undulatory movement [18]; this technique has also been adopted in this study. The thrust force cannot be measured directly using force transducers because the thrust and drag forces are produced in unison while the fish swims [19]. High-resolution digital particle image velocimetry (DPIV) has made it possible to measure the wake in a 2-D plane around or behind the swimming fish. This technique, which was already utilized in our previous investigations on live fish [20] and was also recently applied in an hydrodynamic analysis of a underwater flapping smart material [21], making it possible to estimate the time-averaged thrust force T_f. Many previous studies of the thrust performance of robotic swimmers made use of experimental laboratory models in water tanks. This type of experimental approach allows specific movement patterns and the applications of various measurement techniques [22]–[25] to obtain data such as force, speed, power consumption, and wake flow field.

In this study, we use a novel experimental method to obtain the self-propulsive speed U of a robotic swimmer. The simultaneous measurement of power, external force, and flow visualization data enables calculation of the thrust efficiency. The resulting experimental data are analyzed to elucidate

Manuscript received December 17, 2010; revised May 9, 2011, August 19, 2011, and January 19, 2012; accepted March 27, 2012. Date of publication May 10, 2012; date of current version January 18, 2013. Recommended by Technical Editor J. Wang. This work was supported by National Science Foundation support projects, China, under Contract 61075100.

L. Wen is with the Department of Organism and Evolutionary Biology, Harvard University, Cambridge, MA 02138 USA (e-mail: liwen@oeb.harvard.edu).

T. Wang and J. Liang are with the Robotic Institute, School of Mechanical Engineering and Automation, Beihang University, Beijing 100191, China (e-mail: wtm_itm@263.net; dommy_leung@263.net).

G. Wu is with the State Key Laboratory of Precision Measurement Technology and Instruments, Department of Precision Instruments and Mechanology, Tsinghua University, Beijing 100084, China (e-mail: tophow99@mails.tsinghua.edu.cn).

Color versions of one or more of the figures in this paper are available online at http://ieeexplore.ieee.org.

Digital Object Identifier 10.1109/TMECH.2012.2194719

1083-4435/$31.00 © 2012 IEEE

several important aspects of fish-swimming hydrodynamics. These aspects include not only thrust efficiency, but also the power consumption and wake structure as a function of the Strouhal number (St), a fundamental dimensionless parameter of fish-like locomotion [26]. The remainder of this paper is organized as follows: in Section II, we present materials and methods for the measurement of power and thrust efficiency. In Section III, we introduce the implementation of the experimental apparatus. We present the experimental results in Section IV, followed by relative discussions on the hydrodynamic performance of the robotic fish in Section V. Finally, we summarize current research and findings and present an outline for future studies in Sections VI.

II. Power and Thrust Efficiency of Robotic Fish

A. Robotic Fish Design and Power Measurement

1) Implementation of Robotic Fish: The mackerel (*Scomber scombrus*), a typical carangiform fish that belongs to the BCF swimmers, whose propulsive performance has frequently been investigated by biologists and fluid dynamic researchers, was selected to be the mimic model in our study. The robotic fish was 0.588 m long and consisted of a streamlined main body capable of flexing, and a rigid caudal fin. As can be seen from Fig. 1(a), multilink mechanical skeletons make it possible for the model to have fish-like undulations with the form of an actual fitting curve [27]. The outer shape of the model was an exact replica of the shape of the mackerel, whose body shape parameters were provided by Hess [28]. The illustration Fig. 1(b) provides details of the fabrication. The undulating mechanism was a high-precision assembly of four links made from anodized aluminum and covered with foam and a special waterproof structure made of Silica. Each mechanical link was capable of relative rotation with respect to its neighboring link and was driven by a brush servomotor Maxon RE40 (Maxon Motor, Switzerland), mounted on a metal plate above water. The belts transmitted the motion from the servomotor to each individual transmission shaft (see Fig. 1(c) for notation), ran through the streamlined low-drag vertical strut as shown in Fig. 1(d), and finally drove each individual link to mimic a fish-like undulation. All mechanical links were controlled by a motion coordinator, Trio MC206 (Trio Motion Technology, U.K.).

The kinetic movements for the mackerel are approximately fitted from the observed results by the biologist [28], and can be expressed by the following:

$$h_b(x,t) = a(x)a(t)\sin(kx - \omega t) \tag{1}$$

where

$$a(x) = \begin{cases} 0 & x \le 0.33L \\ c_1\left(\dfrac{x/L - 0.33}{1 - 0.33L}\right) + c_2\left(\dfrac{x/L - 0.33}{1 - 0.33L}\right)^2 & x > 0.33L \end{cases}$$

$$a(t) = \begin{cases} \dfrac{t}{t_0} - \dfrac{1}{2\pi}\sin\left(\dfrac{2\pi t}{t_0}\right) & 0 \le t \le t_0 \\ 1 & t > t_0 \end{cases}. \tag{2}$$

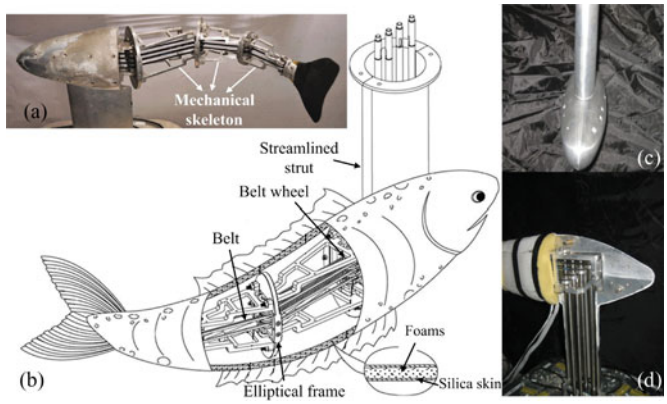

Fig. 1. (a) Snapshot of the mechanical skeleton of a robotic Mackerel. (b) Actuation mechanisms for the relative rotations of the robotic links. (c) Low drag streamlined vertical strut that is connected to the fish's head. (d) Four transmission shafts which run through the streamlined low-drag vertical strut.

$h_b(x,t)$ in (1) denotes the fish kinematics movement function in a body-fixed coordinate system, with the starting point of x measured from the nose of the robotic fish. k denotes the wave number, where $k = 2\pi/\lambda$, and λ denotes the undulating wavelength. ω denotes the circular frequency of oscillation, and $\omega = 2\pi f$. c_1 and c_2 can be adjusted to achieve a specific value for the amplitude envelope of the entire fish body. $L = 0.588$ m, which represents the length of the fish body. From (2), the robotic fish undulates the posterior part (i.e. $x > 0.33\ L$) of the body from rest ($t = 0$) to a steady periodic undulation ($t > t_0 = 1.0\ T$) after a gentle transition process ($0 < t < t_0$). Fig. 2 shows the discrete links that fit the continuous fish body curve. More details of relative techniques can be found in [14] and our previous study [29].

2) Measurement of Power Consumption: The instantaneous total power into the jth motor (link) is

$$P_j(t) = M_j(t)\omega_j(t), j = 1, ...4 \tag{3}$$

where

$$M_j(t) = K_M I_j(t) \text{ and } \omega_i(t) = d(\theta_j(t))/dt$$

where $\omega_j(t)$ denotes the angular speed of the motor at a certain instant. $\omega_j(t)$ is obtained through the differential value of $\theta_j(t)$ of a potentiometer SV01A103 (Murata Manufacturing Company, Ltd., Japan), which is built into the rotation links (as shown in Fig. 3). The torque constant K_M links the mechanical torque M_i with the electric current I_i, which is measured by a Hall effect-based linear current sensor ACS712 (Microsystems Inc., USA) using (3), where $K_M = 0.03$ Nm/A for present actuator Maxon RE40 (Maxon Inc., Switzerland). Fig. 3 shows the circuit measurements across the analog input channels on the Trio-P325 (Trio Motion Technology, U.K.) data acquisition card, with a sampling rate of 200 Hz in this study. The total average power consumption of the fish body within a period can be denoted by the following:

$$P_T = \frac{\int_0^T \sum_{i=1}^{i=4} M_i(t)\omega_i(t)dt}{T} \tag{4}$$

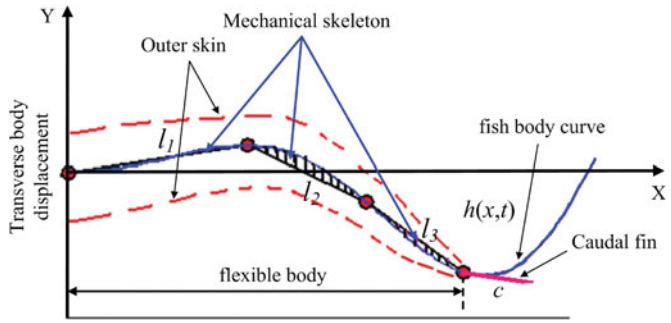

Fig. 2. Schematic view of the robotic mackerel and the discrete links that fitting the curve of the fish body wave.

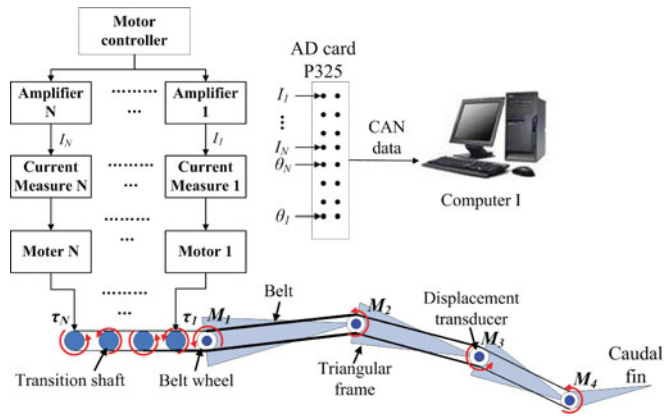

Fig. 3. Schematic view for the robotic fish power measurements, where M_i denotes the bending moment of each discrete joint. The red arrows indicate the rotation of the robotic fish links.

where T denotes the undulating period of the robotic fish. The total power input is given by the integration of four distinct motors.

It should be note that the measured power for the robotic fish while swimming in water includes not only the pure fluid power, but also power losses from the transmission of the robotic mechanism. The pure fluid power consumption is obtained by subtracting the mechanical transmission power from the total power

$$P_{\text{fluid}} = P_T - P_M. \tag{5}$$

Here, P_T and P_M denote the total motor power and mechanical power, and were measured when the robot is undulating in water, and in air, respectively.

To validate the feasibility of the power measurement method and the power accuracy, we conducted the following test. First static torque validation was carried out. As can be seen from Fig. 4, a string passes through the low-friction idler pulley and is attached to one side of the tail of the robotic fish. The performance of the current sensors was examined by applying a known force to the cable, while the servomotors were active in preventing body motion. The data of the current sensors were fully recorded. This test allowed direct comparison of the actual measured force with the theoretical moment of each motor, and comparison results showed that the linearity is better than 2.2%. The dynamic power validation was conducted taking the following steps. Each link of the robotic fish was commanded to make an undulating movement at a preset amplitude and frequency. The current of each link motor was recorded over a precise time of 19 s, and after the initial transients (4 s) had died down, a steady state was achieved by then. The entire dynamic validation test showed that the power measurement had an uncertainty of less than 6%. More detail of the validation process was also described in our previous paper [29].

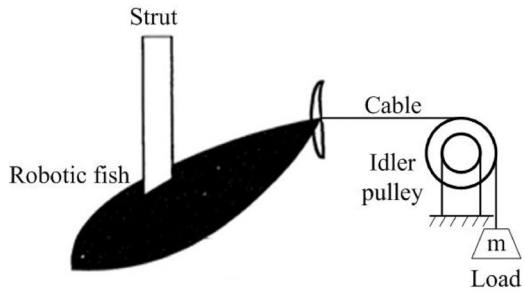

Fig. 4. Schematic view for the external force and power validation.

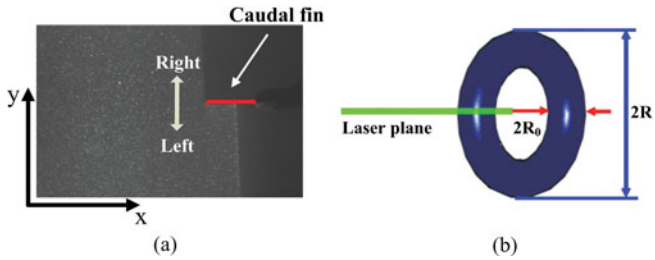

Fig. 5. (a) Captured image of the high-speed CCD camera, where the x-axis is along the fish body direction while the y-axis is along the fish lateral direction. The white dashed box indicates the captured area of the particle images, and the upward and downward flick indicates the side-to-side movement in reality. (b) Schematic view and vorticity parameters of a single 3-D vortex, where the laser sheet passes through the mid depth of the 3-D vortex ring.

B. Measurement of Flow Field and Thrust Force

1) Implementation of the DPIV System: The DPIV system, which was fixed on the carriage, was used to measure the wake flow field that generated by the robotic swimmer, and to estimate the thrust force. The high speed CCD camera (100 fps, 1024 pixels × 1024 pixels, Mintron Inc., Taipei, China) with an optical band pass filter is used to capture the particle images of the flow behind the robotic caudal fin. Simultaneously, the image data will be transferred through a cable to computer II for analysis, a snapshot of the image was shown in Fig. 5(a). The laser beam (4 W) with a wavelength of 0.532 μm is expanded by two cylindrical lenses to generate a light sheet that is reflected successively by three mirrors into the water tank. The wake is visualized by seeding the water with nylon particles (40–70 μm, 1.05 g·cm^{-3}) to reflect the laser light. This resulted in the successful illumination of the captured area by the bright laser light sheet. We then used the "mpiv" MATLAB toolbox, which is open-source software [30] and was also applied to our previous flow measurement of live fish [20].

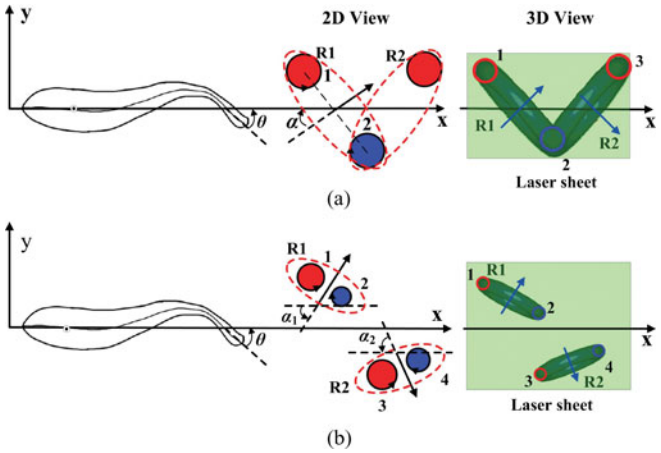

Fig. 6. Schematic views of (a) single-row and (b) double-row vortices in 2-D and 3-D ways. The different colors indicate the distinct directions of vortex rotation, and the arrow indicates the direction of the jet flow.

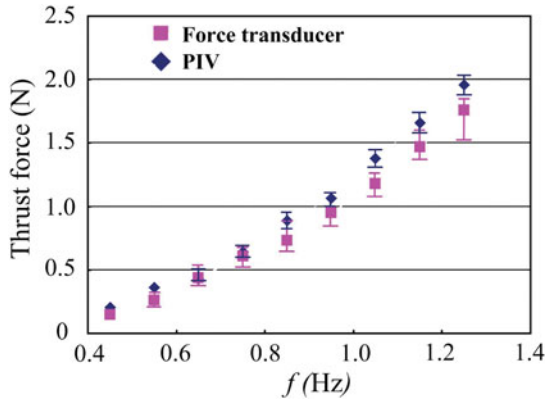

Fig. 7. Thrust force validations at zero towing speed.

The laser sheet plane of the DPIV system is set to pass through the midline of the homocercal caudal fin of the robotic fish. As suggested by biologists, the caudal fin midline was recommended as the best horizontal position for conducting 2-D wake measurements [31]. The depth of 3-D vortex rings (see Fig. 5(b) for notation) was assumed to equals the caudal fin's height, while the measurement planes at other horizontal levels underestimate the thrust force [32].

2) Vortex Dynamic Model of the Thrust Force: In this study, the vortex ring model, which assumes that all the impulse shed by the robotic fish is contained in the elliptical vortex rings, is applied for the analysis of the wake. The measured wake then allows us to use 2-D vortex dynamics theory to compute the impulse. We form the flow field from several tail flap cycles by freezing each vortex in its shed position, and then take measurements of the wake. Previous researchers documented that the robotic fish produced typical reverse Karman vortices [26]. However, there should in fact be two different types of wake structures generated by the robotic swimmer [10]; this point was also later confirmed in the present experiment. The vortex dynamic model and the computing method for these two types of vortices are different. The distribution and morphology of the vortices are demonstrated in Fig. 6 in both 2-D and 3-D views.

Illuminating a cross section through the 3-D vortex ring yields a flow pattern consisting of two vortices. The location of the vortices in the velocity fields was determined by plotting the contours of vorticity. The morphology of a vortex is described by the vortex center, the core radius $R0$, the ring radius R, and the jet angle α (see Fig. 6 for notation). The impulse I of a vortex ring can be calculated by (6) according to the Milne–Thomson principle [33]

$$I = \rho \Gamma A \tag{6}$$

where ρ is the density of water, Γ is the mean absolute value of the circulations of the pair of vortices, and is obtained by the line integration of the tangential velocity component $\overrightarrow{V_T}$ along curve C enclosing the vortex, thus,

$$\Gamma = \oint_C \overrightarrow{V_T} \overrightarrow{dl} \tag{7}$$

where $\overrightarrow{dl}$ is the differential element along the curve C. A is the elliptical area surrounded by the vortex ring that can be derived from the vortex ring radius R and caudal fin height s

$$A = \pi R s/2. \tag{8}$$

The total force was resolved geometrically using the jet angle to determine the axial component of force. For single-row vortices, as can be seen from Fig. 6(a), the vortex rings form a linked chain, and only one vortex ring (i.e., two vortices in the 2-D plane, which are denoted by vortex 1,2) were generated in a flapping circle, and the time-averaged thrust force T_f can be denoted as follows:

$$T_f = If \cos \alpha \tag{9}$$

where f denotes the flapping frequency of the robotic fish. For the double-row vortices (see Fig. 6(b) for notation) the robotic fish generates two vortex rings (i.e., four vortices in the 2-D plane, which are denoted by vortex 1–4) during a flapping circle, the time-averaged thrust force T_f is

$$T_f = I_1 f \cos \alpha_1 + I_2 f \cos \alpha_2 \tag{10}$$

where α_1 and α_2 denote the jet angle for two vortex rings. I_1 and I_2 denote each individual impulse of the vortex ring 1 and 2.

3) Thrust Force Validation: To validate the thrust force that results from the vortex model, the robotic fish was held still at zero towing speed, which enabled it to produce a pure thrust force without drag. In this way, the discrepancy between the force transducer result and vortex model estimation can be evaluated. As shown in Fig. 7, the flapping frequency of the robotic fish was varied systematically and at small increments of 0.1 Hz in the range of 0.4 and 1.2 Hz. As a result, the thrust force estimated by the vortex model was in acceptable agreement with the measurement results of the force transducer. Fig. 8 shows the flow field and wake parameters generated by the robotic fish using a flapping frequency of 0.6 Hz at zero towing speed.

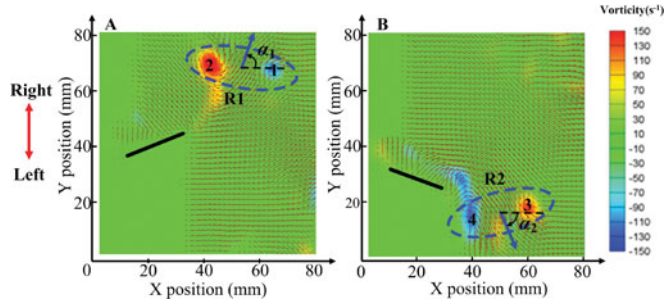

Fig. 8. Flow field and wake parameters generated by a robotic fish in thrust force validation, where the black drawn line indicates the position of the caudal fin of the robotic fish. The vortex numbers are placed near the vortex centers. The direction of left and right flicks of the caudal fin is indicated by the red double-end arrow.

Fig. 8(a) and (b) shows the vorticity and flow vector field at two different times, $T/2$ and T, in a flapping period. The wake structure demonstrated in Fig. 8 can be attributed to double-row vortices, and therefore, thrust force can be calculated according to (10).

III. Experimental Research Apparatus

A. General Experimental Setup

Fig. 9(a) shows the schematic overview of the experimental apparatus. The servo towing system is driven by a 4000 W ac motor, and has a travel distance of 7.5 m, a position accuracy of 0.1 mm, and a maximum speed of 3 ms^{-1}. Underneath the towing system is a water tank measuring 7.8 m × 1.2 m × 1.1 m, in which the robotic fish has sufficient space to move without disturbance from the boundary layer. Furthermore, the robotic fish is forced to move at mid depth in the tank to avoid the interference effect of the free surface and the bottom of the tank. The robotic fish, its motors, and the mechanical transmission mechanism that facilitates power measurement, which were already introduced in Section II-A, are fixed under the force transducer. A low-drag streamlined strut penetrates the water and is connected to the head of the fish.

Varied with conventional free-swimming robotic swimmers, present robotic fish is tethered on the towing system. While the entire body of the robotic fish is submerged in water, the motors and transmission mechanism are mounted on a metal plate and are above the surface. The external force of the robotic fish is measured using a multicomponent piezoelectric force transducer Kislter 9254 C, which is assembled vertically above the robot, and has a natural frequency of 3 kHz, a high rigidity of 500 N/um, and a sensitivity of 0.005 N in the axial direction. The force transducer has two purposes: 1) to help find the self-propulsive speed of the robotic fish and 2) the simultaneous measurement of the lateral force and moment, which will be very useful in future studies. Force calibration results showed that the linearity for the forward force was better than 0.5%, for the lateral force was 0.8%, and for the external moment was 1.0%.

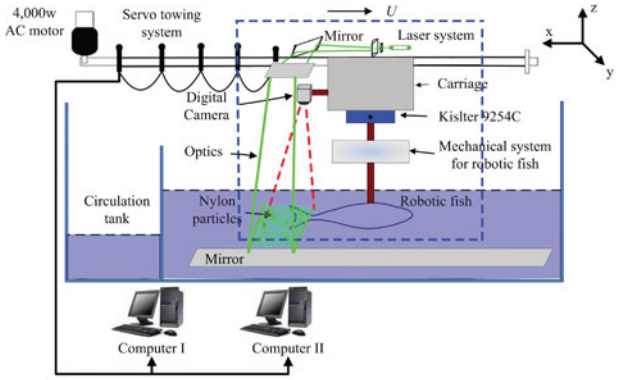

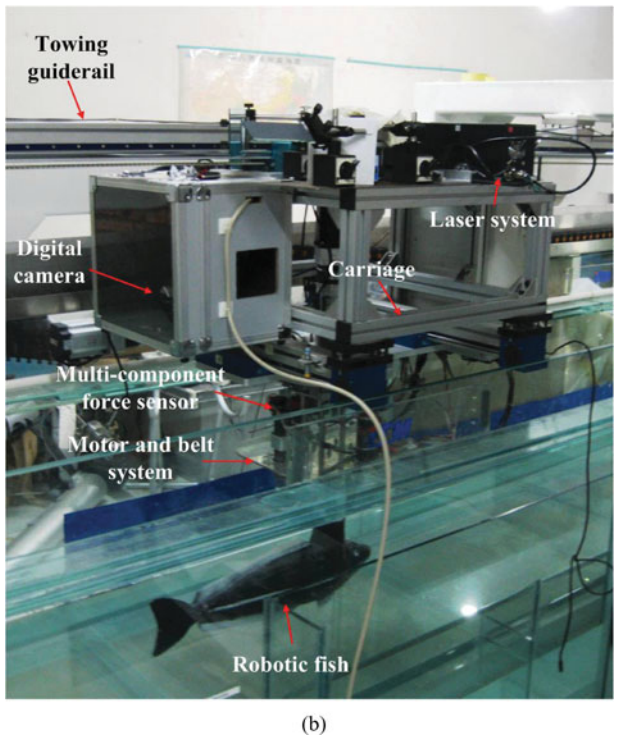

Fig. 9. (a) Schematic overview of the experimental apparatus for the self-propulsive robotic fish. Where the x-axis is along the fish axial direction, the y-axis is along the lateral direction, and the z-axis is selected to be orthogonal to the horizontal plane. (b) Snapshot of the experimental apparatus and the robotic swimmer.

The output of the external Kislter transducer is recorded by a computer through a data cable using a controller area network (CAN) bus. The DPIV system is used to measure the flow field. The particle images are transferred through another data cable to another computer for analysis, capturing the vortex behind the robotic fish. The robotic fish, power measurement system, DPIV system, and force transducers together enable simultaneous recording of the power consumption, the flow field, and the force. A snapshot of the experimental apparatus is also provided in Fig. 9(b). Synchronizing signal from the computer controlling the robotic fish locomotion is used to trigger data acquisition from the Kislter force transducer and also to trigger image acquisition from the high-speed camera. Images of the flow field are, therefore, synchronized with the force and power measurements

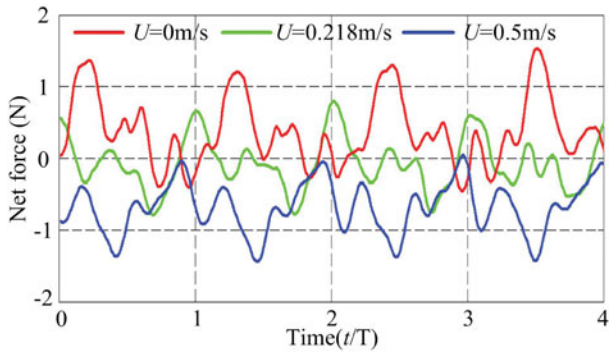

Fig. 10. Instantaneous net axial force measured results at three towing speeds, with the kinetic parameters of the robotic fish: $h = 0.1\ L, f = 0.8$ Hz, $\lambda = 0.95$. See Section II-A for the definitions of the kinetic parameters.

on the robotic fish and with the programmed undulatory movement of robotic fish.

B. Method and Implementation for Self-Propulsion

It is important to note that the self-propulsive speed should be applied under a constant towing speed U when the thrust force is balanced by the drag force, namely, when the average time-average net axial force $\overline{F_x}$ that acts on the robotic fish, measured by the force transducer Kislter 9254 C, is zero. If this equilibrium condition is violated, the robotic fish would accelerate or decelerate under the action of the excess net force. In this study, we fix the robotic fish motion and vary the towing speed U until the time-average net axial force measured by the force transducer is zero. In such a case, the external tether (i.e., the strut in the current apparatus) has no effect on the time-averaged thrust performance. The robotic fish will, therefore, swim at the self-propulsive speed, satisfying the self-propulsion condition.

Fig. 10 shows the time history of the measured instantaneous net axial force F_x at three distinct towing speeds while the robotic fish was programmed to make a certain movement. It can be seen that the net force profile for a given kinematics did not obviously change as the towing speed varied, but the average mean value did. When the towing speed U was set at 0 m/s, the time-average net axial force $\overline{F_x}$ was 0.357 N, i.e., the thrust exceeded the drag force and the net axial force was of a "thrust type." As the towing speed U increased up to a threshold value of 0.218 m/s, $\overline{F_x}$ was -0.006 N. Further increase of U ($U =$ 0.5 m/s) led to a "drag-type" force, where $\overline{F_x} = -0.669$ N. Consequently, the steady mean speed of the robotic fish under the condition of being self-propulsive, where $U = 0.218$ m/s, was in good agreement with the threshold value, which indicated that the time-average net axial force was almost zero. The self-propulsive speed U can, therefore, be determined.

As indicated in previous experimental studies of the flapping foil [26] and the swimming live fish [32], the hydrodynamic performance of fish locomotion is dominated by the fundamental dimensionless parameter—the Strouhal number, which is defined as follows:

$$St = \frac{2fh}{U} \tag{11}$$

where h denotes the undulating amplitude of the caudal fin tip

$$h = |[h_b(x,t)]_{x=L}|_{\max} \tag{12}$$

where $|\cdot|_{\max}$ denotes the maximum absolute value. The Reynolds number Re is defined as follows:

$$\mathrm{Re} = \frac{UL}{v} \tag{13}$$

where L represents the length of the fish, and v represents the kinematic movement viscosity of the water. The mean quantities of force, thrust, power and efficiency are obtained by averaging the instantaneous values over several undulatory cycles of robotic fish. To preserve the relative proportion of the power and thrust force between the present experimental results and previous research works [10], we dimensioned the qualities as follows. The thrust coefficient can be defined as follows:

$$C_T = \frac{T_f}{\rho U^2 L^2} \tag{14}$$

where ρ is the density of the fluid, T is the thrust force estimated by the flow field, see (9) and (10) for notation. U denotes the towing speed of the guide rail. The power coefficient can be denoted by

$$C_P = \frac{P_{\mathrm{fluid}}}{\rho U^3 L^2} \tag{15}$$

where P_{fluid} denotes the time-averaged fluid power (see (5) for notation). Uncertainties in the measured quantities are defined as the standard error of the mean [18]

$$\bar{\sigma} = \sigma/\sqrt{N} \tag{16}$$

where σ is the sample standard deviation for each data point consisting of N measurements, and $N = 5$ in this study. The error bars in all rest figures reflect the uncertainties. The thrust efficiency is defined following Lighthill's papers [9]

$$\eta = T_f U / P_{\mathrm{fluid}}. \tag{17}$$

IV. Experimental Result

Systematic tests were performed for several fixed Strouhal numbers, which were varied in small increments over the range 0.15–1.05. This St range is large enough to cover all prior biological observed results [26]. The undulating beats were cycles of 0.8 Hz in flow with speed of 0.09–0.62 m/s, i.e., $U = 0.09$–0.62 m/s. These operation conditions corresponded to a Re from 5.2×10^4–3.6×10^5, and St ranging over 0.15–1.05; see (13) and (11) for the definitions of Re and St, separately. When the frequency f and amplitude h were preset and held constant, the St can be, therefore, controlled by varying the flow speed U, which is adjusted by the towing system. Recalling previous biological studies, the live mackerel vary their flapping amplitude h as they change their swimming speed U [34]. From the definition of the Strouhal number in (11), in order to keep a constant St value, higher frequency f requires a lower amplitude h; in

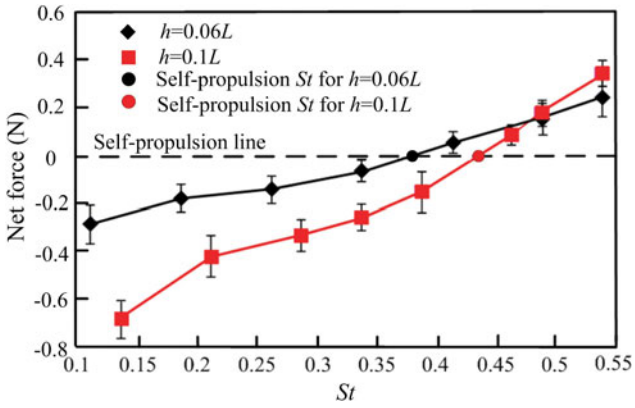

Fig. 11. Mean net force as a function of St for different h—we only provide force data in the St range of 0.15–0.55, where the error bars reflect the measured uncertainties.

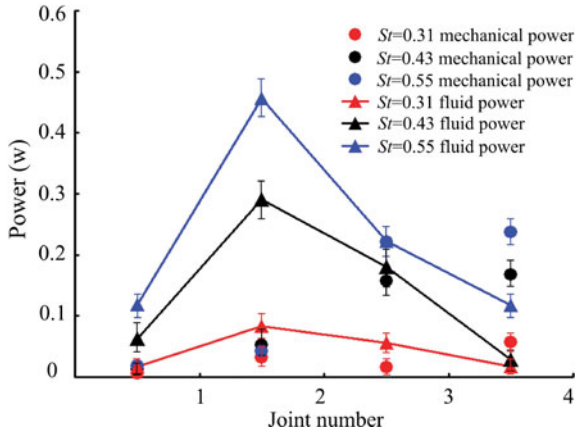

Fig. 12. Power consumption for different links of the robotic fish for varied St.

contrast, a larger amplitude h requires a lower frequency f. An interesting question has been recently posed by both biologists and robotic researchers [14]: while the St is kept constant, which parameter is more sensitive to the thrust performance of robotic (or live) fish, the frequency f or the amplitude h? We are going to investigate this issue in this study.

A. Self-Propulsive Speed

From Fig. 11, as the St increases, the time-average net axial force $\overline{F_x}$ gradually increases from negative to positive values, which share the same trend with that presented in Fig. 11. This phenomenon indicates the transition from a mean drag type net force to a mean thrust type net force. The point at which the $\overline{F_x}$ curve crosses the zero axis (i.e., the self-propulsion line as shown in Fig. 11) indicates the point at which the mean drag force is exactly balanced by the mean thrust force. Therefore, the St at this point is the Strouhal number at which the self-propulsion condition is satisfied. We denote this special St as St*, which indicates the self-propulsion Strouhal number, while the remaining Strouhal numbers are denoted by without the asterisk. For a given flapping frequency f and amplitude h, a larger self-propulsive speed U results in a lower St or St*.

As indicated by biologist [10], there are three principal kinetic parameters in fish locomotion: St, amplitude h, and wavelength λ. In this study, we keep two parameters constant and change the amplitude h from 0.06 L to 0.1 L. From Fig. 12, the absolute value of the higher amplitude ($h = 0.1\ L$) is larger than that of the lower amplitude ($h = 0.06\ L$) at almost the same St by a considerable margin. The case for the lower amplitude h with higher frequency f finally results in a smaller self-propulsion Strouhal number (St$^* = 0.375$) than that of the opposite case (St$^* = 0.43$). Namely, a robotic fish swimming at $h = 0.06\ L$ will be faster than one at $h = 0.1\ L$. As a result, using the self-propulsive swimming speed as a metric, it appears that frequency is more significant than amplitude when St is constrained to a fixed value. In this study, St* can be viewed as a result of the thrust performance of a robotic fish; however, the St* for both amplitudes does not approach the range of Strouhal numbers that most live swimmers achieve in nature ($0.25 < \mathrm{St} < 0.35$) [26]. This reflects the speed disparity between man-made robotic fish and live swimmers.

B. Power Consumption

The mean power for the four discrete mechanical body segments are shown in Fig. 12. The general trend for the power consumption distribution along the axial length of the robotic fish is in accordance with previous experimental biological results, which directly estimated the power consumed by the red muscles along a live mackerel body [34]. It is obvious that the second actuator, which is located at the middle position of a robotic fish, required the most power, while actuators at the remaining positions took less. These results might possibly shed light on the design of robotic fish actuation schemes, by showing that different actuators should be selected to provide the appropriate relative power to the various locations on a robotic fish. In addition, it should be noted that the robotic fish with the belt transmission, the mechanical power P_M (see (5) for notation) of the robotic fish is no more than 22% of the total power P_T. Therefore, the belt transmission approach may provides a better way to drive the fish body than using steel wire [19], by using which the mechanical power loss came to 47% of the total power.

Fig. 13 shows the plot of the power coefficient C_p (see (15) for notation) versus Strouhal number, the relationship between C_p and St can be well described by a third-order polynomial. It is clearly evident that the C_p increases with St, and C_p for $h = 0.1\ L$ is larger by a good margin than that for $h = 0.06\ L$ for the same St. In a previous computational study, Borazjani and Sotiropoulos [10] predicted a C_p of 0.0136 at Re $= 4000$, and $C_p = 3.95 \times 10^{-4}$ under inviscid conditions, i.e., Re $= \infty$, where ∞ represents infinity. As pointed out by previous researchers [9], the power coefficient C_p decreases as Re increases. The measured result of a C_p of 3.39×10^{-3} at Re $= 1.28 \times 10^5$ is well between the values of C_p for Re $= 4000$ and Re $= \infty$. Since the experimental data of previous research on power coefficients are limited, more systematic comparison cannot be carried out. However, the only existing prior study by Borazjani suggests that the present result for the power coefficient is quite reasonable.

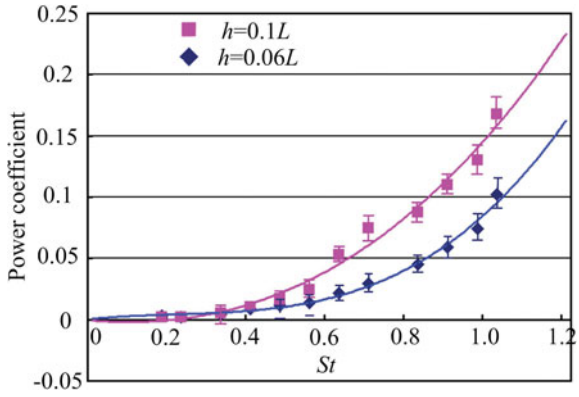

Fig. 13. Power coefficient versus St as a function of amplitude h.

C. Wake Flow Field and Thrust Force

1) Wake Flow Field: Fig. 14(a)–(d) shows the DPIV time-series of the flow field at the self-propulsive Strouhal number (i.e., $St^* = 0.43$) for $h = 0.1\ L$. Within a flapping cycle, the tail performed a flick to its right side and then another to its left, and each flick of the tail generated a vortex ring. As shown in Fig. 14(b), vortices 1 and 2 were generated from the right side flick (toward the left) and formed the vortex ring R1, which is denoted by the red dashed enveloped line. From Fig. 14(d), vortices 3 and 4 were generated from the left side flick (toward the right) and formed the vortex ring R2. The vortex rings R1 and R2 are characterized by lateral divergence and then spread away from the body axis in a wedge-like arrangement. Considering the large-scale characteristics of the wake structure, this type of flow field is dubbed "double-row street" and it has previously been observed in this study of the finite flapping foils by Buchholz and Smits [18]. In comparison, the flow field in Fig. 15(a)–(d) at St = 0.325 shows that the wake structure is quite similar to that of a live swimming mackerel [31]. For such a case, the vortices are organized in a single row structure, and only one vortex ring is generated in a tail beat, while the two vortices in the 2-D plane were located on different sides of the body axis and moved backward. Combined with previous wake structure study on the flapping foils [11], this type of wake flow can be dubbed the typical "reverse Karman street."

Recent computational and biological results indicate that the wake structure of fish locomotion depends primarily on St [10], [11]. Present experimental results suggest that the wake generated by a robotic fish that is an exact replica of a live mackerel is "double-row street" within $0.325 < St < 1.025$. While for $0.15 \leq St \leq 0.325$, we find the typical "reverse Karman street." The schematic view of these two types of wake structure can be referred to Fig. 6. To the best of our knowledge, it is the first time the wake pattern transition has been observed for a whole robotic swimmer at varied St. It should be noted that the current robotic fish traveling at a self-propulsive speed for both amplitudes ($h = 0.06\ L$ and $h = 0.1\ L$) turn out to generate a "double-row" wake flow pattern. The main reason for this result may due to the fact that the robotic fish swims at relatively high Strouhal numbers, $St^* = 0.375$ and 0.43 for $h = 0.06\ L$ and $0.1\ L$, respectively. The shedding vortices from the caudal fin, therefore, tend to have a larger lateral velocity component, which advects them away from the midline of the body and causes them to spread in a lateral direction. As a result, the wake splits laterally and the "double-row" wake structure emerges.

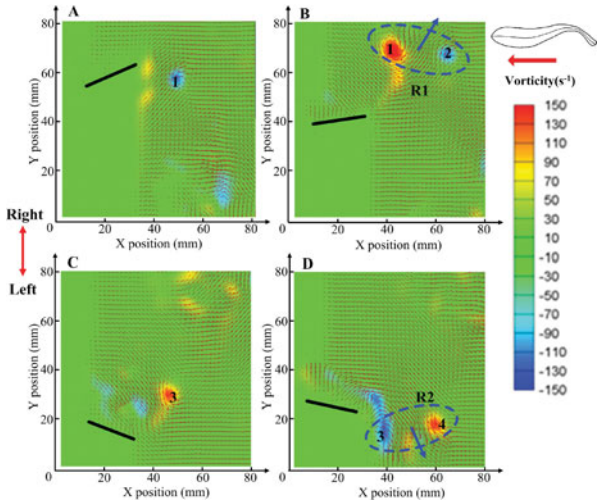

Fig. 14. Double row vortex, recorded at St = 0.43, the black drown line represent the position of the flapping caudal fin. The direction of left and right flicks of the caudal fin is indicated by the red double-end arrow.

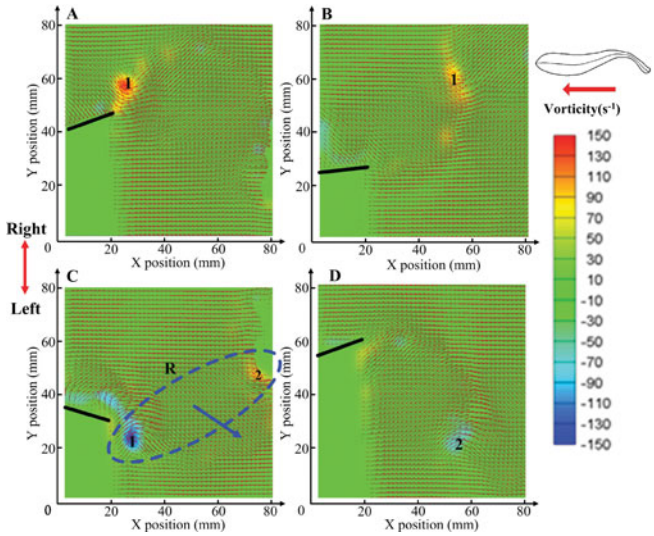

Fig. 15. Single row "reverse Karman vortex," recorded at St = 0.325.

2) Estimated Thrust Force: As mentioned, the time-averaged thrust force can be computed from (9) or (10), and the thrust coefficient C_T is defined in (14). The relationship between C_T and St for both amplitudes is well-fit by second-order polynomials as shown in Fig. 16. The value of C_T for $h = 0.1\ L$ is larger by a well margin than that for $h = 0.06\ L$ at the same St.

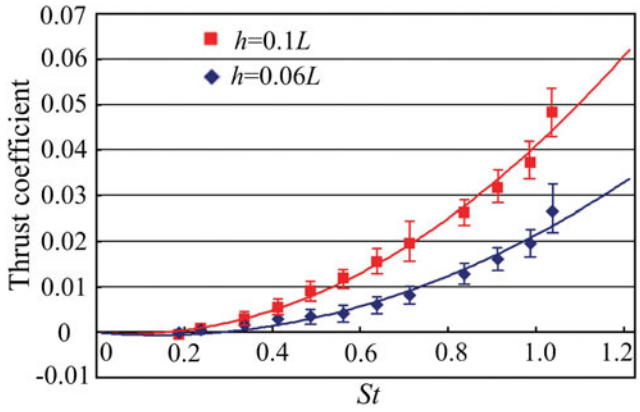

Fig. 16. Thrust coefficient versus St as a function of the amplitude h.

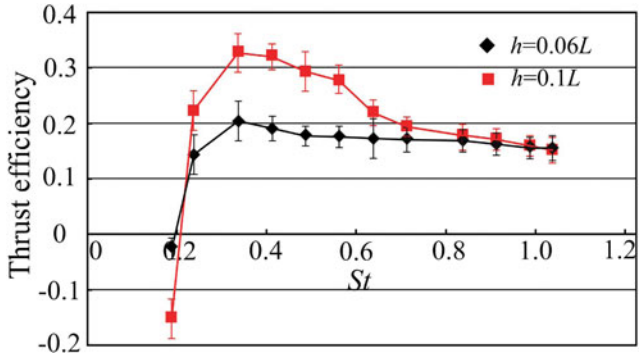

Fig. 17. Thrust efficiency versus St for varied amplitudes h.

D. Result of Thrust Efficiency

Fig. 17 shows the thrust efficiency η as a function of St for both amplitudes ($h = 0.06\ L$ and $h = 0.1\ L$). The principal findings that follow Fig. 17 can be summarized as follows.

1) The optimal thrust efficiency for both amplitudes fell within the range of $0.3 \leq \mathrm{St} \leq 0.325$. Beyond this optimal region, the thrust efficiency decreases drastically with decreasing St, and negative thrust efficiency appeared at $\mathrm{St} = 0.15$. The maximum thrust efficiency recorded in this study is 32.8%, centered on $h = 0.1\ L$, $\mathrm{St} = 0.325$, while the thrust efficiency decreased gradually with increasing St within the range $0.35 < \mathrm{St} \leq 1.025$. At an amplitude of $0.06\ L$ (i.e., $h = 0.06\ L$), a peak thrust efficiency of 20.4% was recorded at $\mathrm{St} = 0.325$, while for the case of $h = 0.1\ L$, the peak thrust efficiency of 32.8% also appeared at $\mathrm{St} = 0.325$. The measurement uncertainties of the thrust efficiency, which are represented by the error bars, are not significant.

2) Taking into account the thrust efficiency at the self-propulsive strouhal number(St^*), the robotic fish with larger amplitude is more efficient than the one with low amplitude, by a large margin. A relatively higher self-propulsive speed can be achieved at lower amplitude. Namely, high thrust efficiency and large self-propulsion speed might not be produced at the same time at the same amplitude h. This result actually agrees well with Read's [12] study on the infinite flapping foil and Smits' [18] investigations on a finite flapping flat plate with low aspect ratio.

3) In summary, both the thrust efficiency and wake structure are closely related to St. At the optimal efficiency region within $0.3 \leq \mathrm{St} \leq 0.325$, the wake structure presents as a single-row "reverse Karman street," which is located well within the St range of efficient-swimming live Mackerel ($0.25 < \mathrm{St} < 0.35$). However, the self-propulsive Strouhal number St^* for both amplitudes ($\mathrm{St}^* = 0.375$ for $h = 0.06\ L$, $\mathrm{St}^* = 0.43$ for $h = 0.1\ L$) is beyond the optimal region. In such cases, robotic fish produced relatively lower thrust efficiency (for the quantitative value see Table I) and generated another type of wake structure, the "double-row" wake pattern.

Recalling previous studies, the thrust efficiency is mainly calculated by using a mathematical model such as Lighthill's elongate body theory (EBT) [9], or directly from the results of 3-D numerical simulations [10], [40]. The thrust efficiency based on the EBT [9] can be denoted as follows:

$$\eta = \frac{1}{2}(1+\beta) \tag{18}$$

where $\beta = U/V_b$, and $V_b = \lambda f$. Here, β denotes the slip velocity defined as the ratio of the self-propulsion speed U of the robotic fish, to the undulation wave speed V_b of the fish body. The improved EBT efficiency formula [35], which takes into account the slope angle effect of fish caudal fin, can be expressed as follows:

$$\eta = \frac{1}{2}(1+\beta) - \frac{1}{2}\gamma^2(\beta^2/1+\beta) \tag{19}$$

where

$$\gamma = \left[\frac{tg|\theta(x,t)|_{\max}}{|h_b(x,t)|_{\max}} \times \frac{\lambda}{2\pi}\right]_{x=L}. \tag{20}$$

θ represents the slope angle of the caudal fin (see Fig. 7 for notation). θ can be expressed as follows:

$$\theta(x,t) = dh_b(x,t)/dt. \tag{21}$$

In Table I, the quantitative thrust efficiencies are provided using various approaches, including EBT, improved EBT, 3-D CFD, and present experimental results. To the best of our knowledge, there were very limited papers reported the experimental results on thrust efficiency for a BCF undulatory robotic swimmer. Flapping foils have often been applied to mimic fish fins when considering their thrust performance during locomotion [19]. The existing prior results on thrust efficiency are mainly based on the infinite and finite flapping foils [11], [18]. The experimental results of flapping foils are, therefore, included in Table I for comparison.

V. Discussion

In this study, techniques of DPIV and mechatronics are applied to the measurement of the thrust efficiency of a biomimetic robotic fish. Using the present experimental method, the robotic swimmer is mounted on a servo towing system and can find its self-propulsive speed by the measured force acting upon it. The thrust efficiency of the robotic fish was obtained by simultaneously measuring the power, flow field and self-propulsion speed. The generality of this measurement approach, discussed in this paper, indicates that many broader issues of biologically

TABLE I
EXPERIMENTAL THRUST EFFICIENCY RESULTS AND THE COMPARISON WITH PREVIOUS STUDIES

Variable	Symbol	EBT	Improved EBT	Infinite foil	Finite foil	CFD -1	CFD -2	*St**-1 Exp.	*St**-2 Exp.
Strouhal number	*St*	0.43	0.43	0.43	0.43	0.61	0.25	0.43	0.375
Aspect Ratio	*AR*	∞	∞	6	2.38	2.68	2.68	2.68	2.68
Reynolds number	*Re*	∞	∞	4×10^4	3.2×10^4	4×10^3	∞	1.28×10^5	8.9×10^4
Amplitude	*h/c*	0.773	0.773	0.75	0.75	0.773	0.773	0.773	0.464
Thrust efficiency (%)	η	74.5	62.5	61	22	22.5	45	31.6	18.6

inspired underwater robotic experiments can be conducted using the method, such as the robotic pectoral fin [37], multifin undulation [8], [22], and some other unsteady fluid propulsion [38].

It is important to comment on the comparison of thrust efficiency between previous studies and current experimental results. We first compared the present efficiency values with EBT and improved the EBT methods of self-propulsive Strouhal number St^*. Although the improved EBT method takes slope angle effect into account and was proved to be more accurate for estimating the thrust efficiency of carangiform fish, it is apparent that the improved EBT method still yields larger values than the present experimental results. As reported in both biological and computational papers [10], [36], even if EBT and improved EBT methods provide simple and easy calculations for thrust efficiency, both methods overestimate it. This overestimation is largely due to the fact that both methods are inviscid (i.e., $\mathrm{Re} = \infty$ as denoted in Table I) slender-body theory. They do not take the viscous effect into account, and are, therefore, not an adequate comparison to the present situation.

Then, we consider the discrepancy in thrust efficiency between biomimetic flapping foils and robotic fish. It should be noted that the infinite flapping foil [11] denoted here is actually the flapping foil with a high aspect ratio ($\mathrm{AR} = 6$), while the AR of the finite foil is 2.38 [18], which is very close to the aspect ratio of the robotic mackerel's caudal fin. At the self-propulsion Strouhal number ($\mathrm{St}^* = 0.43$), it is obvious that the thrust efficiency of an infinite flapping foil ($\eta = 61\%$) is higher than that of the robotic fish and of a finite flapping foil, but the efficiency of a finite flapping foil ($\eta = 22\%$) approximates to the results of a robotic fish. As indicated by Buchholz [18], this discrepancy is mainly due to the 3-D fluid effect, and the thrust efficiency decreases as the aspect ratio is decreased. Recently the rapid development of 3-D-CFD has provided a more scientific approach for calculating the thrust efficiency, in which the 3-D, viscous and unsteady flow effects are all seriously considered computationally. As reported in Table I, Borazajani computed a thrust efficiency of 22% at $\mathrm{Re} = 4000$ and 45% at $\mathrm{Re} = \infty$. As indicated by previous researchers [10], [32], the thrust efficiency η increases as Re increases. This experiment results in a thrust efficiency of $\eta = 32.8\%$ at $\mathrm{Re} = 1.28 \times 10^5$ for $\mathrm{St}^* = 0.43$, which is reasonable and shows good agreement with the results of the 3-D-CFD results.

Present experimental results showed some disparities of hydrodynamics between the robotic swimmer and the live fish. As addressed by biologists, thrust performance of fish is evaluated by self-propulsive swimming speed (in this study we use St^*) and thrust efficiency [1]. The self-propulsive Strouhal numbers of present robotic mackerel are 0.43 and 0.375 for $h = 0.1\ L$ and $h = 0.06\ L$, separately. They are higher than the Strouhal number of the live fish ($0.25 < \mathrm{St} < 0.35$). According to the definition of St in (11), the Strouhal number can be viewed as a result of the self-propulsive speed of the robotic swimmer. The disparity between the St for robotic and live swimmers, therefore, reflects the gap between swimming speeds of the swimmers. As DPIV results additionally demonstrated, the large-scale characteristics of the flow patterns generated by the robotic swimmer with both amplitudes ($h = 0.06\ L$ and $h = 0.1\ L$) kinematics were double-row wake structures—also shows some difference with those produced by live fish [31].

The engineers are eager to enhance the thrust performance of robotic fish. It is important to note that, in addition to the St and amplitude h that we considered in this paper, there are other parameters that could potentially affect the fish-swimming performance. For instance, the wavelength λ is fixed to $0.95\ L$ in this study, whereas the wavelength of the BCF swimmer is between the range of $0.64\ L < \lambda < 1.25\ L$. As reported in numerous previous literature [19], [39], a larger wavelength would decrease the swimming drag, which in turn affects St^* and thrust efficiency, therefore it is apparent that the effect of wavelength should be seriously considered. Also, here the body and tail of robotic fish are treated together as a single undulating wave for simplicity. However, recent biological findings indicate that the caudal fin undergoes complex kinematics independent of the body in mackerel and tuna [32], [34], which will naturally affect the thrust performance. Noting this, more principal parameters besides the current kinetic parameters will be examined in our future studies; these parameters include the caudal fin pitch angle θ and body wavelength λ, with the aim of exploring better thrust performance in biomimetic robotic swimmers.

VI. CONCLUSION AND FUTURE STUDIES

In this study, we experimentally measured the thrust efficiency of a BCF undulatory robotic fish. We showed that the optimal thrust efficiency region is within the Strouhal number range of $0.3 \leq \mathrm{St} \leq 0.325$, when the wake structure produced robotic fish is of the form of single-row "reverse Karman vortices." Nevertheless, with most parameter combinations, the self-propulsive Strouhal numbers St^* were outside the optimal region. In these cases, relatively lower thrust efficiencies were recorded and another type of wake structure was observed: the "double-row vortices". We also showed that while keeping St constant, a higher self-propulsive speed can be achieved by coupling a low amplitude with a large flapping frequency. In

contrast, the robotic fish can reach higher thrust efficiencies when a larger amplitude is paired with a lower frequency. Quantitative experiment results showed that when $h = 0.06\ L$, the thrust efficiency is 18.6% recorded at $\mathrm{St}^* = 0.375$, while when the amplitude increased to $h = 0.1\ L$, a higher thrust efficiency of $\eta = 31.6\%$ can be achieved at $\mathrm{St}^* = 0.43$.

Systematic investigation of the parametric dependence of more principal parameters including St number, amplitude, caudal fin pitch angle, and body wavelength on the thrust performance of robotic fish will be conducted in our future study.

ACKNOWLEDGMENT

The authors would like to thank Prof. G. V. Lauder for his kind and helpful suggestions on our experimental apparatus. They would also like to thank C. Witt and G. Walker of the Lauder Laboratory who contributed greatly to the improvement of this manuscript, and J. Li, Z. Fan, and L. Bao for providing help in implementing the experimental apparatus and conducting the experiments.

REFERENCES

[1] G. V. Lauder, "Swimming hydrodynamics: Ten questions and the technical approaches needed to resolve them," *Exp. Fluids*, vol. 51, pp. 23–35, 2011.
[2] S. Guo, "A new type of fish-like underwater microrobot," *IEEE/ASME Trans. Mechatronics*, vol. 8, no. 1, pp. 136–141, Mar. 2003.
[3] Y. Zhang *et al.*, "Design optimization of a bidirectional microswimming robot using giant magnetostrictive thin films," *IEEE/ASME Trans. Mechatronics*, vol. 14, no. 4, pp. 493–503, Aug. 2009.
[4] Z. Chen *et al.*, "Modeling of biomimetic robotic fish propelled by an ionic polymer—Metal composite caudal fin," *IEEE/ASME Trans. Mechatronics*, vol. 15, no. 3, pp. 448–459, Jun. 2010.
[5] M. Aureli, "Free-locomotion of underwater vehicles actuated by ionic polymer metal composites," *IEEE/ASME Trans. Mechatronics*, vol. 15, no. 4, pp. 603–614, Aug. 2010.
[6] T. Wang, L. Wen, J. Liang, and G. Wu, "Fuzzy vorticity control of a biomimetic robotic fish using a flapping lunate tail," *J. Bion. Eng.*, vol. 7, no. 3, pp. 56–65, 2010.
[7] J. Yu, R. Ding, Q. Yang, M. Tan, W. Wang, and J. Zhang, "On a bio-inspired amphibious robot capable of multimodal motion," *IEEE/ASME Trans. Mechatronics*, [Online]. Available: ieeexplore.ieee.org, DOI: 10.1109/TMECH.2011.2132732.
[8] C. Zhou and K. H. Low, "Design and locomotion control of a biomimetic underwater vehicle with fin propulsion," *IEEE/ASME Trans. Mechatronics*, vol. 17, no. 1, pp. 25–35, Feb. 2012.
[9] M. J. Lighthill, "Large-amplitude elongated-body theory of fish locomotion," *Proc. R. Soc. Lond. B*, vol. 179, pp. 125–138, 1971.
[10] I. Borazjani and F. Sotiropoulos, "Numerical investigation of the hydrodynamics of carangiform swimming in the transitional and inertial flow regimes," *J. Exp. Biol.*, vol. 211, pp. 1541–1558, 2008.
[11] J. M. Anderson, K. Streitlien, and D. S. Barrett, "Oscillating foils of high propulsive efficiency," *J. Fluid Mech.*, vol. 360, pp. 41–72, 1998.
[12] D. A. Read, F. S. Hover, and M. S. Triantafyllou, "Forces on oscillating foils for propulsion and maneuvering," *J. Fluids Struct.*, vol. 17, pp. 163–183, 2003.
[13] C. M. Breder, "The locomotion of fishes," *Zoologica*, vol. 4, pp. 159–297, 1926.
[14] J. Yu, M. Tan, S. Wang, and E. Chen, "Development of a biomimetics robotic fish and its control algorithm," *IEEE Trans. Syst. Man Cybern. B, Cybern.*, vol. 34, no. 4, pp. 1798–1810, Aug. 2004.
[15] R. Madangopal *et al.*, "Energetic-based design of small flapping-wing micro air vehicles," *IEEE/ASME Trans. Mechatronics*, vol. 11, no. 4, pp. 433–438, Aug. 2006.
[16] S. H. McIntosh *et al.*, "Design of a mechanism for biaxial rotation of a wing for a hovering vehicle," *IEEE/ASME Trans. Mechatronics*, vol. 11, no. 2, pp. 143–153, Apr. 2006.
[17] E. Steltz *et al.*, "Dynamometer power output measurements of miniature piezoelectric actuators," *IEEE/ASME Trans. Mechatronics*, vol. 14, no. 1, pp. 1–10, Feb. 2009.
[18] J. H. J. Buchholz and A. J. Smits, "The wake structure and thrust performance of a rigid low-aspect-ratio pitching panel," *J. Fluid Mech.*, vol. 603, pp. 331–365, 2008.
[19] D. S. Barrett, M. S. Triantafyllou, and D. K. P. Yue, "Drag reduction in fish-like locomotion," *J. Fluid Mech.*, vol. 392, pp. 183–212, 1999.
[20] G. Wu, Y. Yang, and L. Zeng, "Kinematics, hydrodynamics and energetic advantages of burst-and-coast swimming of koi carps (*Cyprinus carpio koi*)," *J. Exp. Biol.*, vol. 210, pp. 2181–2191, 2007.
[21] S. D. Peterson *et al.*, "A particle image velocimetry study of vibrating ionic polymer metal composites in aqueous environments," *IEEE/ASME Trans. Mechatronics*, vol. 14, no. 4, pp. 474–483, Aug. 2009.
[22] G. V. Lauder, E. J. Anderson, J. Tangorra, *et al.*, "Fish biorobotics: Kinematics and hydrodynamics of self-propulsion," *J. Exp. Biol.*, vol. 210, pp. 2767–2780, 2007.
[23] D. N. Beal and P. R. Bandyopadhyay, "A harmonic model of hydrodynamic forces produced by a flapping fin," *Exp. Fluids*, vol. 43, no. 5, pp. 675–682, 2007.
[24] K. Morgansen, V. Duindam, R. Mason, J. Burdick, and R. Murray, "Nonlinear control methods for planar carangiform robot fish locomotion," in *Proc. IEEE Int. Conf. Robot. Autom.*, 2001, pp. 427–434.
[25] F. Liu, K.-M. Lee *et al.*, "Hydrodynamics of an undulating fin for a wave-like locomotion system design," *IEEE/ASME Trans. Mechatronics*, vol. 17, no. 3, pp. 554–562, Jun. 2012.
[26] M. S. Triantafyllou, G. S. Triantafyllou, and D. K. P. Yue, "Hydrodynamics of fish-like swimming," *Annu. Rev. Fluid Mech.*, vol. 32, pp. 33–53, 2000.
[27] J. Yu and L. Wang, "Parameter optimization of simplified propulsive model for biomimetic robot fish," in *Proc. IEEE Int. Conf. Robot. Autom.*, Barcelona, Spain, Apr. 2005, pp. 3317–3322.
[28] F. Hess and J. J. Videler, "Fast continuous swimming of saithe (*Pollachius virens*): A dynamic analysis of bending moments and muscle power," *J. Exp. Biol.*, vol. 109, pp. 229–251, 1984.
[29] L. Wen *et al.*, "Hydrodynamic experimental investigation on efficient swimming of robotic fish using self-propelled method," *Int. J. Offshore Polar Eng.*, vol. 20, no. 3, pp. 167–174, 2010.
[30] N. Mori and K. Chang, Introduction to MPIV–PIV toolbox in MATLAB-version 0.965 [EB/OL]. (12-21-2004) [Online]. Available: http://sauron.urban.eng.osaka-cu.ac.jp/∼mori/softwares/mpiv
[31] J. C. Nauen and G. V. Lauder, "Hydrodynamics of caudal fin locomotion by chub mackerel, Scomber japonicus (Scombridae)," *J. Exp. Biol.*, vol. 205, pp. 1709–1724, 2002.
[32] F. E. Fish and G. V. Lauder, "Passive and active flow control by swimming fishes and mammals," *Annu. Rev. Fluid Mech.*, vol. 38, pp. 193–224, 2006.
[33] L. M. Milne-Thompson, *Theoretical Aerodynamics*. New York: Macmillan, 1966.
[34] J. M. Donley and K. A. Dickson, "Swimming kinematics of juvenile kawakawa tuna (*Euthynnus affinis*) and chub mackerel (*Scomber japonicus*)," *J. Exp. Biol.*, vol. 203, pp. 3103–3116, 2000.
[35] J.-Y. Cheng, "Note on the calculation of propeller efficiency using elongated body theory," *J. Exp. Biol.*, vol. 192, pp. 169–177, 1994.
[36] E. D. Tytell and G. V. Lauder, "The hydrodynamics of eel swimming—I. Wake structure," *J. Exp. Biol.*, vol. 207, pp. 1825–1841, 2004.
[37] J. L. Tangorra, G. V. Lauder *et al.*, "The effect of fin ray flexural rigidity on the propulsive forces generated by a biorobotic fish pectoral fin," *J. Exp. Biol.*, vol. 213, pp. 4043–4054, 2010.
[38] P. C. Strefling, A. M. Hellum, and R. Mukherjee, "Modeling, simulation, and performance of a synergistically propelled ichthyoid," *IEEE/ASME Trans. Mechatronics*, vol. 17, no. 1, pp. 36–45, Feb. 2012.
[39] A. H. Techet, "Separation and turbulence control in biomimetic flows," *Flow, Turbul. Combust.*, vol. 71, pp. 105–118, 2003.
[40] Q. Zhu, M. J. Wolfgang, and D. K. P. Yue, "Three-dimensional flow structures and vorticity control in fish-like swimming," *J. Fluid Mech.*, vol. 468, pp. 1–28, 2002.

Li Wen received the B.S. degree in mechanical engineering from Beijing Institute of Technology, Beijing, China, in 2005, and the Ph.D. degree from the Department of Mechanical Engineering and Automation, Beihang University, Beijing, China, in 2011.

He is currently a Postdoctoral Researcher in the Lauder Laboratory, Harvard University, Cambridge, MA. His current research interests include bioinspired robotics, experimental fluid mechanics, microfabrication, and biomechanics.

Dr. Wen has served as the Session Chair for several academic conferences, including the IEEE/RSJ International Conference on Intelligent Robots and Systems and IEEE International Conference on Robotics and Automation. He was also the recipient of the Best Student Paper Award from the International Society of Offshore and Polar Engineers in 2010.

Tianmiao Wang received the B.S. degree from Xian Jiaotong University, Xian, China, in 1982 and the M.S. and Ph.D. degrees from Northwestern Polytechnical University, Xian, in 1985 and 1990, respectively.

He is currently the Dean and a Professor in the School of Mechanical Engineering and Automation, Beihang University, Beijing, China. He is the Head of the expert group in the field of advanced manufacturing technology of the National High Technology Research and Development Program (863 Hi-Tech Program). He has undertaken and finished many national research projects in recent years. He had published nearly 87 papers in local and international journals and three professional books. His research interests include biomimetic robotics, medical robotic technology, and embedded intelligent control technology.

Dr. Wang is a member of the China Robotics Society.

Guanhao Wu received the B.S. degree in measurement and control technology and instrumentation and the Ph.D. degree in optical engineering from Tsinghua University, Beijing, China, in 2003 and 2008, respectively.

He is currently an Assistant Professor in the Department of Precision Instruments and Mechanology, Tsinghua University. His research interests include bionic study of fish and insects, light detection, and ranging. He is the author/coauthor of more than ten refereed journal articles and about ten conference papers. He is the holder of six Chinese patents.

Jianhong Liang received the Bachelor's and Ph.D. degrees in mechanical engineering and automation from Beihang University, Beijing, China.

He is currently an Assistant Professor in the School of Mechanical Engineering and Automation, Beihang University. He has published nearly 40 papers in native and international journals and two professional books, and also received many awards. His research interests include biomimetic underwater robotics, field robotics, and small unmanned robotic systems.